

3D fusion of intravascular ultrasound and coronary computed tomography for in-vivo wall shear stress analysis: a feasibility study

Alina G. van der Giessen · Michiel Schaap · Frank J. H. Gijsen · Harald C. Groen · Theo van Walsum · Nico R. Mollet · Jouke Dijkstra · Frans N. van de Vosse · Wiro J. Niessen · Pim J. de Feyter · Antonius F. W. van der Steen · Jolanda J. Wentzel

Received: 19 February 2009 / Accepted: 26 October 2009 / Published online: 28 November 2009
© Springer Science+Business Media, B.V. 2009

Abstract Wall shear stress, the force per area acting on the lumen wall due to the blood flow, is an important biomechanical parameter in the localization and progression of atherosclerosis. To calculate shear stress and relate it to atherosclerosis, a 3D description of the lumen and vessel wall is required. We present a framework to obtain the 3D reconstruction of human coronary arteries by the fusion of intravascular ultrasound (IVUS) and coronary computed tomography angiography (CT). We imaged 23 patients with IVUS and CT. The images

from both modalities were registered for 35 arteries, using bifurcations as landmarks. The IVUS images together with IVUS derived lumen and wall contours were positioned on the 3D centerline, which was derived from CT. The resulting 3D lumen and wall contours were transformed to a surface for calculation of shear stress and plaque thickness. We applied variations in selection of landmarks and investigated whether these variations influenced the relation between shear stress and plaque thickness. Fusion was successfully achieved in 31 of the 35

Electronic supplementary material The online version of this article (doi:[10.1007/s10554-009-9546-y](https://doi.org/10.1007/s10554-009-9546-y)) contains supplementary material, which is available to authorized users.

A. G. van der Giessen · F. J. H. Gijsen (✉) · H. C. Groen · A. F. W. van der Steen · J. J. Wentzel
Department of Biomedical Engineering, Erasmus MC, Biomechanics Laboratory Ee2322, PO Box 2040, 3000 CA Rotterdam, The Netherlands
e-mail: f.gijsen@erasmusmc.nl

M. Schaap · T. van Walsum · N. R. Mollet · W. J. Niessen · P. J. de Feyter
Department of Radiology, Erasmus MC, Rotterdam, The Netherlands

J. Dijkstra
Department of Radiology, Leiden University Medical Center, Leiden, The Netherlands

P. J. de Feyter
Department of Cardiology, Erasmus MC, Rotterdam, The Netherlands

A. G. van der Giessen · F. N. van de Vosse
Department of Biomedical Engineering, Eindhoven University of Technology, Eindhoven, The Netherlands

A. F. W. van der Steen
The Interuniversity Cardiology Institute of the Netherlands, Utrecht, The Netherlands

M. Schaap · T. van Walsum · W. J. Niessen
Department of Medical Informatics, Erasmus MC, Rotterdam, The Netherlands

W. J. Niessen
Faculty of Applied Sciences, Delft University of Technology, Delft, The Netherlands

arteries. The average length of the fused segments was 36.4 ± 15.7 mm. The length in IVUS and CT of the fused parts correlated excellently ($R^2 = 0.98$). Both for a mildly diseased and a very diseased coronary artery, shear stress was calculated and related to plaque thickness. Variations in the selection of the landmarks for these two arteries did not affect the relationship between shear stress and plaque thickness. This new framework can therefore successfully be applied for shear stress analysis in human coronary arteries.

Keywords Coronary · CT · IVUS · Wall shear stress · Registration · Atherosclerosis

Abbreviations

CT	Computed tomography
IVUS	Intravascular ultrasound
WSS	Wall shear stress
PT	Plaque thickness
LAD	Left coronary artery
RCA	Right coronary artery
LCX	Left circumflex artery
95% CI	95% Confidence interval
MPR	Multiplanar reformat

Introduction

Although the wall shear stress (WSS), the force per area acting on the lumen wall due to the blood flow, is small compared to the pressure, it is an important biomechanical parameter in the localization and progression of atherosclerosis [1, 2]. WSS induces processes on cellular and molecular level that influence the atherogenicity of the vessel wall [3]. It has also been demonstrated that WSS is an important factor in the generation of the vulnerable plaque [4] and it has been hypothesized that it plays a role in plaque destabilization [5]. WSS is thus an important parameter to study in relation to atherosclerosis. Since WSS is hard to measure accurately in the coronary arteries, the WSS is assessed by computational fluid dynamics [6]. These computations need the 3D geometry of the coronary lumen. To relate the WSS to the atherosclerotic plaque size,

also the 3D geometry of the coronary wall is necessary.

Coronary CT angiography is a very promising 3D imaging modality to visualize the coronary arteries, detect significant stenosis [7, 8] and rule out coronary disease [9]. Some studies already showed that WSS calculations are possible in CT derived geometries [10–12]. However, accurate delineation (manually or automatically) of the lumen is still challenging and good discrimination of the vessel wall is even harder [13–16]. Thus, CT is yet not a suitable stand-alone imaging modality for studying the relation between WSS and atherosclerosis.

The gold standard for coronary lumen and wall information is intravascular ultrasound (IVUS) [17]. However, IVUS is a 2D technique that does not provide the 3D information that is required to generate a geometry of the lumen to calculate WSS. In this paper we present a framework to fuse the accurate lumen and wall information from IVUS and the 3D information from CT to obtain the 3D geometry of the coronary lumen and wall that can be used as input for the WSS calculations. The fusion of IVUS and CT is validated by comparing the length of IVUS and CT. In addition, we demonstrate the robustness of the framework by introducing variations in the fusion procedure and discussing the effect of these variations on WSS analysis.

Methods

Patients

We retrospectively included 23 patients who were treated for coronary artery disease in our institution. Patients were included in case an IVUS pullback was performed in one or more of the coronary arteries and in addition underwent coronary CT angiography shortly before or after the interventional procedure. Exclusion criteria to perform coronary CT angiography were renal failure, contrast allergy, irregular heart rate, contra-indications to β -blockade and the inability to hold breath for 15 s. A single oral dose of 100 mg metoprolol was administered 45 min prior to scanning to patients with a heart rate higher than 70 beats min^{-1} to improve CT image quality [18, 19]. Patients were

excluded from this study if they had prior bypass surgery. Arteries that were treated were excluded. All patients gave informed consent and the institutional review board approved the study protocols.

CT acquisition

Scanning was performed on a 64-slice CT scanner (Sensation64[®], Siemens, Germany). A detailed description of the patient preparation, scan protocol and image reconstruction has previously been described [8]. Briefly, a contrast enhanced scan (Iomeron 400[®], Braco, Italy) was performed according to a standardized optimized contrast-enhanced scanning protocol. The initiation of the scan was synchronized to the arrival of contrast in the coronary arteries by a bolus-tracking technique. The images were reconstructed initially during the mid-to-end diastolic phase (350 ms prior to the *R*-wave) with a temporal window of 165 ms. Whenever the image quality was poor, more reconstructions were made at different phases of the cardiac cycle, and the best reconstruction was selected.

IVUS acquisition and analysis

During the interventional procedure one or more of the main coronary arteries of the patients were imaged with IVUS. Patients received ≥ 200 μg of intracoronary nitroglycerine before acquisition. A motorized pullback was performed at 0.5 mm s^{-1} with a commercial available 40 MHz IVUS catheter (Atlantis SR Pro, Boston Scientific, Boston, MA). The pullback was started >10 mm distal of the segment of interest and ended at the aorta-ostial junction. The images acquired just before systole were extracted from the complete pullback based on an ECG gating method [20]. The distance between the extracted images depended on the heart rate of the patient during the pullback and was ~ 0.5 mm. The lumen and external elastic membrane (EEM) contours were semi-automatically delineated on the IVUS images with a validated software package (QIVUS, Medis, Leiden, The Netherlands) according to international standardized guidelines [17]. This software package provides a initial segmentation of the lumen and the EEM and allows manual corrections afterwards. The center of the lumen was determined for each cross-section by

calculating the center of mass C_i of each lumen contour.

Fusion IVUS and CT

The goal of the fusion of IVUS and CT was to reconstruct the 3D position and orientation of the IVUS-derived lumen and media contours. We used MeVisLab (Mevis, Bremen, Germany) to build a software tool for the fusion of IVUS and CT and for the visualization.

An IVUS stack encompasses a set of n 2D images $I_i \in [1:n]$. We used the CTA data and corresponding 3D central lumen line to semi-manually determine for each of these 2D images I_i the 3D center of mass of the lumen C_i , the normal of the 3D plane N_i , and a vector pointing in the positive *y*-direction of the 2D IVUS image U_i . The different steps of the fusion process are explained in detail below.

1. Annotation of the central lumen line:

We manually annotated the central lumen line by placing points approximately every 1–2 mm points in the center of the artery as determined by the three orthogonal views of the CT dataset. The annotation started at the ostium and ended as distally as possible. A curved multi-planar reformat (MPR) image is generated along the centerline to judge the quality of the centerline and, if necessary, to improve it. The centerline markers were smoothed and resampled for each 0.2 mm.

The smoothed centerline is used in the fusion as follows; the IVUS center of mass C_i is positioned somewhere on the centerline, N_i corresponds to the tangent of the centerline at the respective position, and the orientation vector U_i is perpendicular to N_i . The manual interaction is used to determine the two remaining degrees of freedom for each IVUS image; the 1D centerline position (resulting in C_i and N_i) and the angle of rotation around the centerline (resulting in U_i).

2. Matching of landmarks on IVUS and CT:

The 1D centerline positions of $C \triangleq \{C_1, \dots, C_n\}$ were determined in a two-step approach. First we manually defined the positions for a set of landmark IVUS images I_i . As landmarks the bifurcations seen on IVUS and CT were used. Guided by the distance between the bifurcations in the IVUS image stack and their appearance, we searched in a stack of

cross-sectional MPR CT images (Fig. 1a) for the same bifurcations as were identified on IVUS images. This stack of MPR CT images consists of images generated at every 0.2 mm of and perpendicular to the central lumen line. For each matched bifurcation that was found we selected the image from the IVUS stack which showed the carina of the bifurcation of interest. The image from the MPR CT stack was selected which showed the carina in the same way (Fig. 1b). The 1D position on the central lumen line of each the matching MPR CT images was assigned to its matched IVUS image resulting in the positions for C_i . This was done for all bifurcations found both in IVUS and CT and for at least two bifurcations per artery. The second step is determining the position of the remaining IVUS images between the landmark IVUS images. These were achieved by linear interpolation of the 1D positions of the landmark images. Thus the position of C and the normals $N \triangleq \{N_1, \dots, N_n\}$ of the IVUS images are now known.

3. Determining rotation angle:

Using the semi-manually determined positions of C and normals $N \triangleq \{N_1, \dots, N_n\}$ the software tool reformatted a set of MPR CT images, with each MPR CT image corresponding to one IVUS image.

For each matched bifurcation we then rotated the selected IVUS image around the center of the lumen in such way that the bifurcation had the same orientation as the bifurcation on CT (see Fig. 1b), resulting in an orientation vector U_i for each landmark image I_i . The orientations of intermediate IVUS images were determined by spherical linear interpolation (<http://portal.acm.org/citation.cfm?doid=325334.325242>).

The resulting set of 3D IVUS image poses and the associated contours are subsequently used to create the 3D lumen and vessel wall geometry of the coronary artery (see Fig. 1c–d).

Length validation

To validate the fusion procedure we compared the length of each fused artery for IVUS and CT. On IVUS the length was calculated by multiplying the number of fused images by the averaged distance in between the images as was calculated during the ECG based extraction of the images. In the CT data, the length of the centerline between the first and last CT landmark was computed.

Wall shear stress analysis

For two coronary arteries we calculated the WSS in the 3D geometries derived from the fusion procedure and related the WSS to the plaque thickness. We selected two extremes from the database; one very diseased artery with significant stenotic areas and calcifications in the artery wall and one mildly diseased artery with only minimal diffused wall thickening without calcifications. From the 3D IVUS contours a lumen and wall surface was generated and smoothed (Laplacian 0.2 smoothing factor, ten smoothing passes, with boundary and border preservation). The lumen surface was meshed with $\sim 800,000$ linear tetrahedral elements with an edge-size of 0.1 mm on the wall (Gambit 2.4.6, Fluent Inc. Products, ANSYS, Inc., USA). The WSS was calculated by simulating a 3D incompressible and laminar flow (FIDAP 8.7.4, Fluent Inc. Products, ANSYS, Inc., USA). We assumed the blood to be non-Newtonian (Carreau model with time constant = 25 s, power law index = 0.25, zero-viscosity = 0.25 kg ms^{-1} and infinity-viscosity = $0.0035 \text{ kg ms}^{-1}$ [21]) with a density of $1,050 \text{ kg m}^{-3}$. We estimated the inlet flow by assuming a WSS of 0.6 Pa [22] at the walls and calculated the corresponding inlet flow by Poiseuille's Law. This flow was prescribed at the inlet by a parabolic flow profile. WSS was calculated in a post-processing step using FieldView (FieldView 10F, Intelligent Light, Lyndhurst, USA). For more details on the computational methods we refer to Krams et al. [6].

The plaque thickness is calculated by determining the shortest distance from the lumen surface to the wall surface [Vascular Modeling Toolbox (www.vmtk.org)]. Subsequently the lumen surface is opened along the length of the lumen, and the WSS and plaque thickness values are mapped onto a 2D surface as is shown in Fig. 5. Each pixel represents 0.5 mm of the arteries length and 10° angle and all values within this pixels are averaged. To obtain the relation between the WSS and the plaque thickness, both the WSS and the plaque thickness are averaged over the length of the artery as was described by Krams et al. [6] (Matlab 7.1, The MathWorks, Inc., Natick, MA, USA). The WSS-plaque-thickness linear relation can now be determined by regression analysis [23] and is described as:

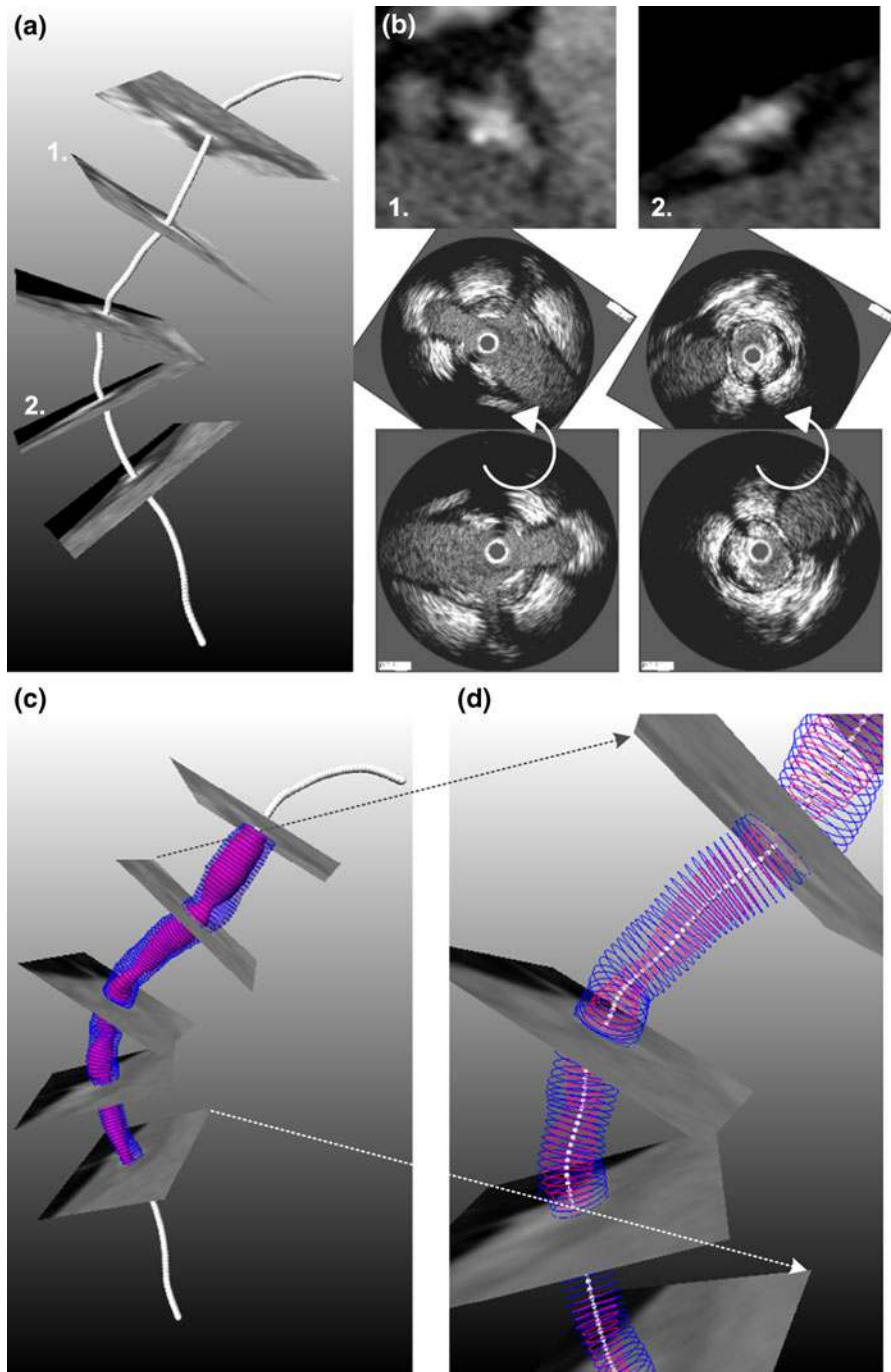


Fig. 1 Fusion. **a** Shows the centerline of in the very diseased artery. Perpendicular to this centerline every 0.2 mm cross-sectional images were generated. In these images we searched for the landmarks that we found on IVUS. The CT images that were matched to the five landmarks found on IVUS are shown in three dimensions. In **b** two of the five matched landmarks are

depicted: at the top the landmarks in CT and at the bottom the landmarks on IVUS. Rotation is applied to the IVUS images to obtain the correct orientation (middle panel). **c** Shows the IVUS contours placed on the CT derived centerline together with the CT landmarks. A magnification of the 3D contours is shown in **d**

$$\overline{PT}(\phi) = a\overline{WSS}(\phi) + b,$$

with \overline{WSS} , the WSS averaged over the length (Pa), \overline{PT} , the plaque thickness averaged over the length (mm), ϕ the radial position and (a) (mm Pa^{-1}) and (b) (mm) the regression parameters.

Effect of landmark selection

The 3D reconstruction of the lumen and vessel wall can be influenced by observer dependent choices in the fusion procedure, especially for the selection and rotation of the landmarks; a CT image more proximal or distal can be appointed as match to the landmark IVUS image and also the rotation applied to orient the IVUS images can be user-dependent. For both the very diseased and the mildly diseased artery, we varied the matching of the IVUS landmarks to the CT images and the rotation as depicted in Fig. 2 and we looked into the influence on the WSS and PT analysis.

First we varied the selection of the CT image that is matched to the IVUS image containing the landmark, thus introducing a longitudinal variation. Instead of the original matched CT image, we selected for the second landmark a CT image 2 slices (0.4 mm) more proximal and for the third landmark we selected a CT image, 2 images (0.4 mm) more distal to the original matched CT image. Secondly, we varied the rotation angle for the second landmark and third landmark by changing the rotation angle 5° in opposite direction for the second and third landmark. Finally the previous variations in longitudinal and angular direction were combined as a worst case scenario for mismatching. Similarly to the original fusion, for these three variations the IVUS contours were placed into 3D, WSS and plaque thickness were calculated and the WSS-plaque-thickness relation was determined. Subsequently the WSS and plaque thickness of these variations were compared to the original matching on a pixel-to-pixel basis. By Blant–Altman analysis we determined 95% confidence interval (CI) of the differences between the original and each of the varied fusions. We also identified the location of the maximum plaque thickness and showed how the location of the maximum PT and the WSS at this point is influenced by the variations in matching. The regression parameters of the WSS-plaque-thickness relation were

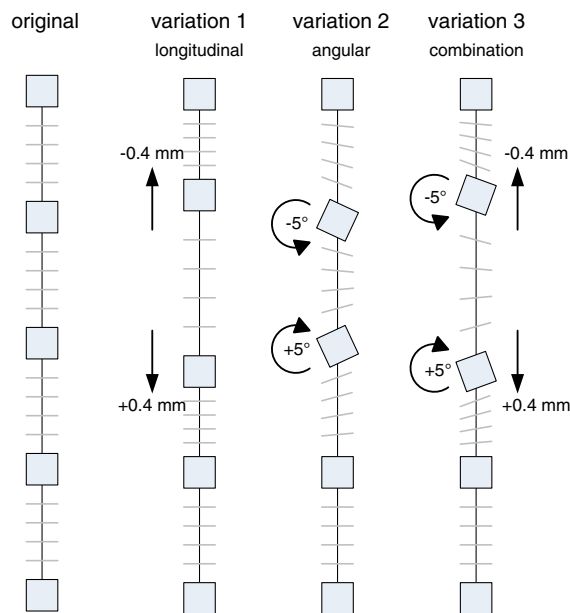


Fig. 2 Variations in landmark selection. The squares depict the IVUS landmarks that are matched to the CT landmarks. On the left, the original landmarks for the fusion of IVUS and CT are depicted. We applied three variations on the fusion. For the longitudinal variation 1, IVUS landmark 2 is positioned 0.4 mm (two slices) more proximal on the CT centerline and landmark 3 is positioned 0.4 mm (two slices) more distal. For angular variation 2, we changed the rotation of the matched IVUS landmark image around the CT centerline. Landmark 2 was rotated 5° counter clockwise and landmark 3 was rotated 5° clockwise. Variation 3 is the combination of the previous two variations. Note how these variations influence the distribution of the IVUS contours between the landmarks

calculated also for the variations and compared to the regression parameters of the original matching.

Results

Fusion

We included 35 arteries (12 LAD, 13 LCX, 10 RCA) from 23 patients in our study. We were not able to fuse IVUS and MSCT for four arteries (three LCX and one RCA) because not enough matching landmarks were found on both IVUS and CT. On average IVUS and CT were fused over a length of 36.4 ± 15.7 mm by on 3.7 (2–7) landmarks per artery. The number of landmarks and fusion length was not different for the three main coronary arteries (Kruskal–Wallis test, $P > 0.05$).

Length validation

Regression analysis showed a good linear relationship between the IVUS and CT length with $R^2 = 0.98$ (see Fig. 3a). The averaged length of the fused part was 5.1% longer on CT than on IVUS (36.4 ± 15.7 vs. 38.2 ± 16.4 mm, paired *t*-test, $P < 0.05$) with a 95% CI from 17.5 to -7.4% (0.95 – 2.66 mm) (see Fig. 3b). The relative difference in length was not larger for the LCX (9.0%) than for the LAD (3.5%) and RCA (2.8%) (Kruskal–Wallis, $P > 0.05$) (see Fig. 3c).

Wall shear stress analysis

The fusion of the very diseased artery, an LAD, is visualized in Fig. 1. This artery was fused with five landmarks over a length 54.5 mm with 111 IVUS images. Besides the validation in length also visual inspection of matched IVUS and cross-sectional CT images (see Movie in “Supplementary material”) and the delineation of the IVUS contours on CT as depicted in Fig. 4 indicate a successful fusion process. Calculations of flow through this diseased artery showed WSS values ranging from 0.3 to 6.0 Pa (mean 1.1 ± 1.0 Pa), see Fig. 5. The plaque thickness varied over the artery from 0.2 to 2.5 mm (mean: 0.9 ± 0.4 mm). WSS peaks were observed at the stenotic sites and coincide with the sites with the largest plaque thickness. The WSS and plaque thickness were positively correlated ($R^2 = 0.77$, $a = 1.5$ Pa mm $^{-1}$ and $b = -0.8$ Pa).

The mildly diseased RCA was fused over a length of 40.6 mm with four landmarks. The plaque thickness ranged from 0.5 ± 0.2 mm (0.1 – 1.1 mm),

which is clearly smaller than for the very diseased artery. The WSS pattern showed no peak values due to stenotic sites as in the diseased artery. The WSS varied between 0.3 and 0.9 Pa (mean 0.5 ± 0.1 Pa). The WSS-plaque-thickness showed no linear relation ($R^2 = 0.04$, $a = -1.3$ Pa mm $^{-1}$ and $b = 1.2$ Pa) (see Fig. 6). All these parameters confirm that this artery is indeed without extensive atherosclerotic disease.

Effect of landmark selection

The WSS patterns for the variations are very similar (Fig. 7). The averaged WSS value, as well as the minimum and maximum WSS values do not change due to the variation in landmark selection. The strictest way to evaluate the impact of the variations is comparing the differences on a pixel-to-pixel basis as is depicted for the diseased artery in Fig. 8. At pixel level we found that 95% of the WSS differences were -0.45 to $+0.40$ Pa for the longitudinal variation, -0.12 to $+0.10$ Pa for the angular variation and -0.45 to $+0.40$ Pa for the combined variation (see also Table 2). The Bland–Altman plot to compare the original fusion with the combined variation is depicted in Fig. 9. The angular variation had no additional influence over the longitudinal variation.

As for the WSS patterns also the plaque thickness patterns look very similar (Fig. 7). Also the averaged PT over the complete artery the plaque thickness was similar for the original and varied fusions, but, as seen for the WSS, locally the difference can be large, especially near the stenotic sites (Fig. 8). The plaque thickness differed on a pixel-to-pixel basis between

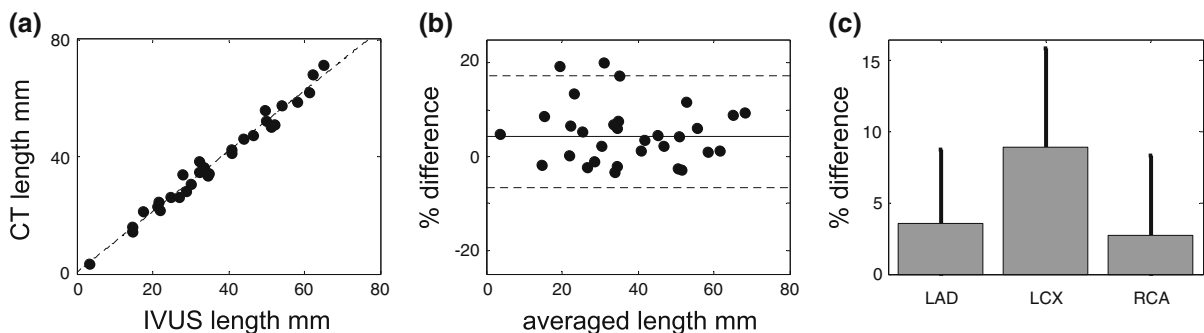


Fig. 3 Length validation. **a** Regression plot; **b** Bland–Altman plot; **c** Difference per artery. Error bars indicate the standard deviation

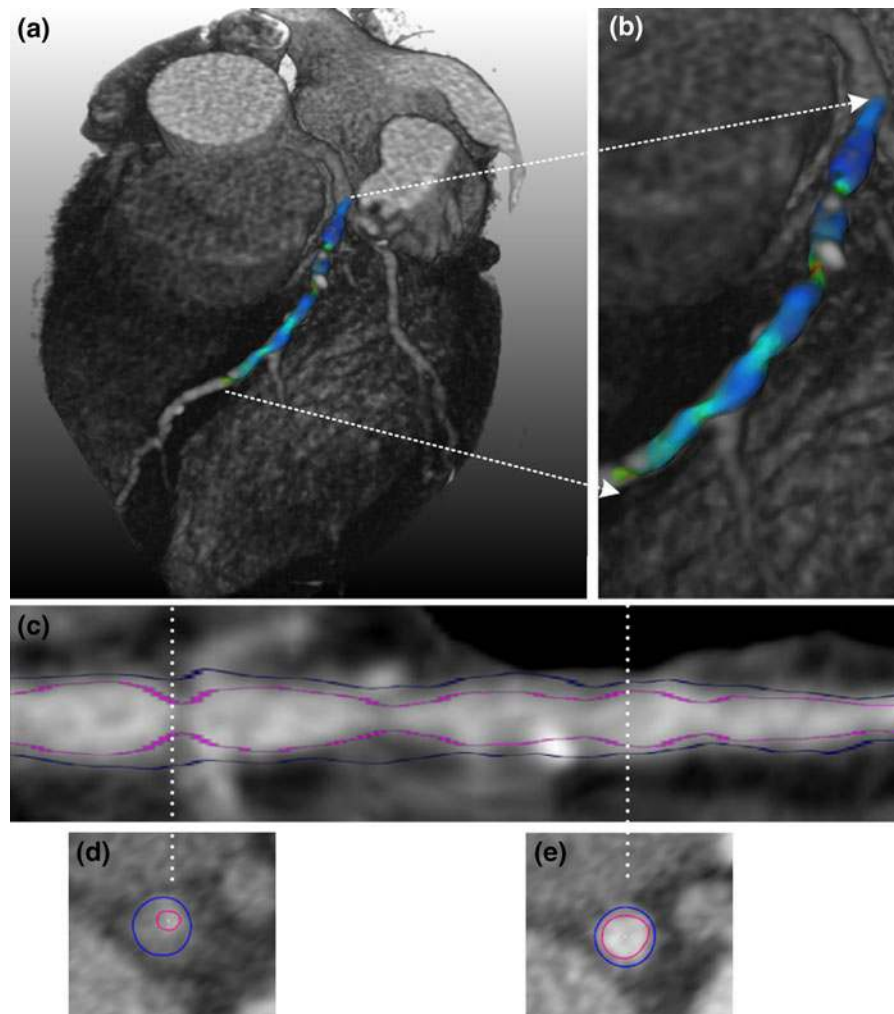


Fig. 4 IVUS fused in CT. **a** 3D CT dataset of the heart fused with the IVUS derived geometry of the lumen on which the calculated WSS values are depicted. **b** Magnification of panel 1. **c** CT curved multi-planar reformatted image along the

centerline of the diseased artery with the fused lumen (pink) and wall (blue) IVUS contours. **d, e** Cross-sectional CT images at the indicated locations with the fused lumen (pink) and wall (blue) IVUS contours

−0.13 and +0.12 mm (95% CI) due to longitudinal variation, between −0.05 and +0.06 (95% CI) due to the angular variations and between −0.14 and 0.14 mm (95% CI) for the variations combined (see also the Bland–Altman plot in Fig. 9). Table 1 shows that due to the variations, the location of the maximum PT did hardly change, however, the WSS was 0.4 Pa, 17%, less for variation 3.

The WSS-plaque-thickness-relation is hardly influenced by applying variations in the fusion (see Fig. 8); R^2 was 0.74, 0.71 and 0.76, (a) was 1.4, 1.5 and 1.5 and (b) was −0.7, −0.8 and −0.8

for the longitudinal, angular and combined variations.

In the mildly diseased artery the averaged WSS and plaque thickness patterns were very similar for the original fusion and the variations (Fig. 7). Also the averaged WSS and PT values did not change due to any of the variations. The WSS and plaque thickness did change locally, but with lower absolute difference than for the very diseased artery (Fig. 10). As for the diseased artery the influence of the angular variation was less for both the WSS and plaque thickness. For the combined most severe variation the

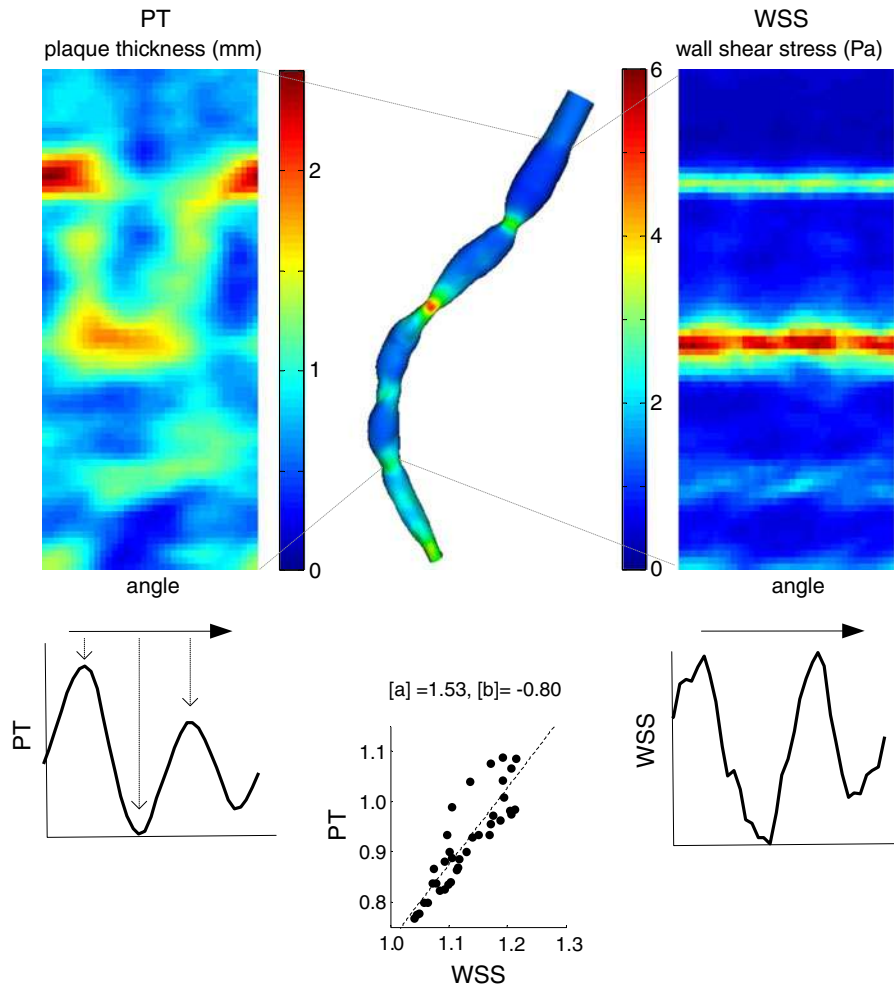


Fig. 5 Wall shear stress analysis for the diseased artery. The wall shear stress (WSS) of the very diseased artery is depicted at the 3D lumen wall in the center. The WSS (right image) and plaque thickness (PT) (left image) can be displayed as a 2D image by virtually cutting open and unfolding the artery along its length. To obtain the WSS-PT-relation, both are averaged

over the length of the artery, as can be seen in the left and right panels below the WSS and PT map. These longitudinally averaged values are plotted and by regression analysis the relationship between WSS and PT can be determined, **a** indicates the slope and **b** the off-set

WSS differed -0.04 to $+0.05$ Pa (95% CI). For the plaque thickness the differences were between the -0.06 to $+0.06$ mm (95% CI) (see also the Bland–Altman plots in Fig. 9). Because the WSS and plaque thickness was on average low in the healthy artery the relative changes are large (Table 2), however, Table 1 shows that the variations have no influence on the location of the maximum PT and the WSS at the maximum PT location. Also for this mildly diseased artery the WSS-plaque-thickness relation did hardly change (R^2 was 0.04, 0.05 and 0.04, (a)

was -1.2 , -1.6 and -1.3 and (b) was 1.2, 1.4 and 1.2 for the longitudinal, angular and combined variations.

Discussion and conclusions

In this manuscript a framework to generate 3D coronary lumen and wall geometries by fusion of CT and IVUS data of human coronary arteries is presented for the first time. The results of the current study show that this new accurate and robust method

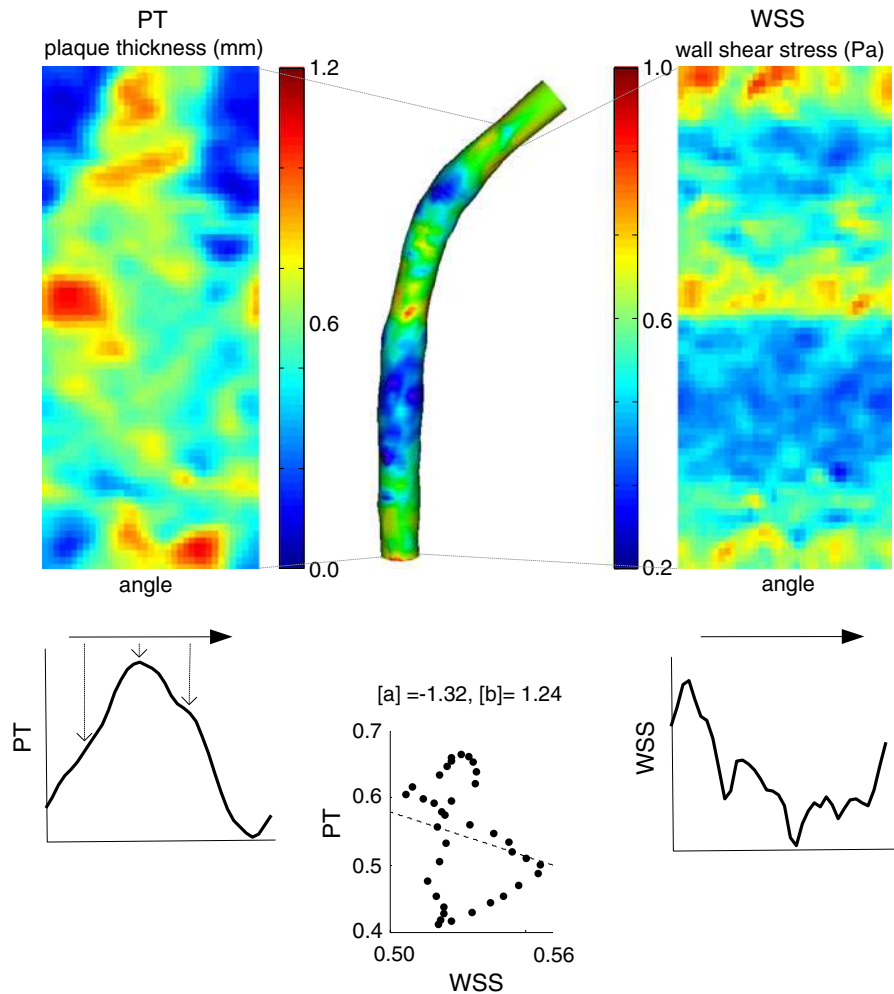


Fig. 6 Wall shear stress (WSS) analysis for the mildly diseased artery. The WSS of the mildly diseased artery is depicted at the 3D lumen wall in the center. The WSS (right image) and plaque thickness (PT) (left image) can be displayed as a 2D image by virtually cutting open and unfolding the

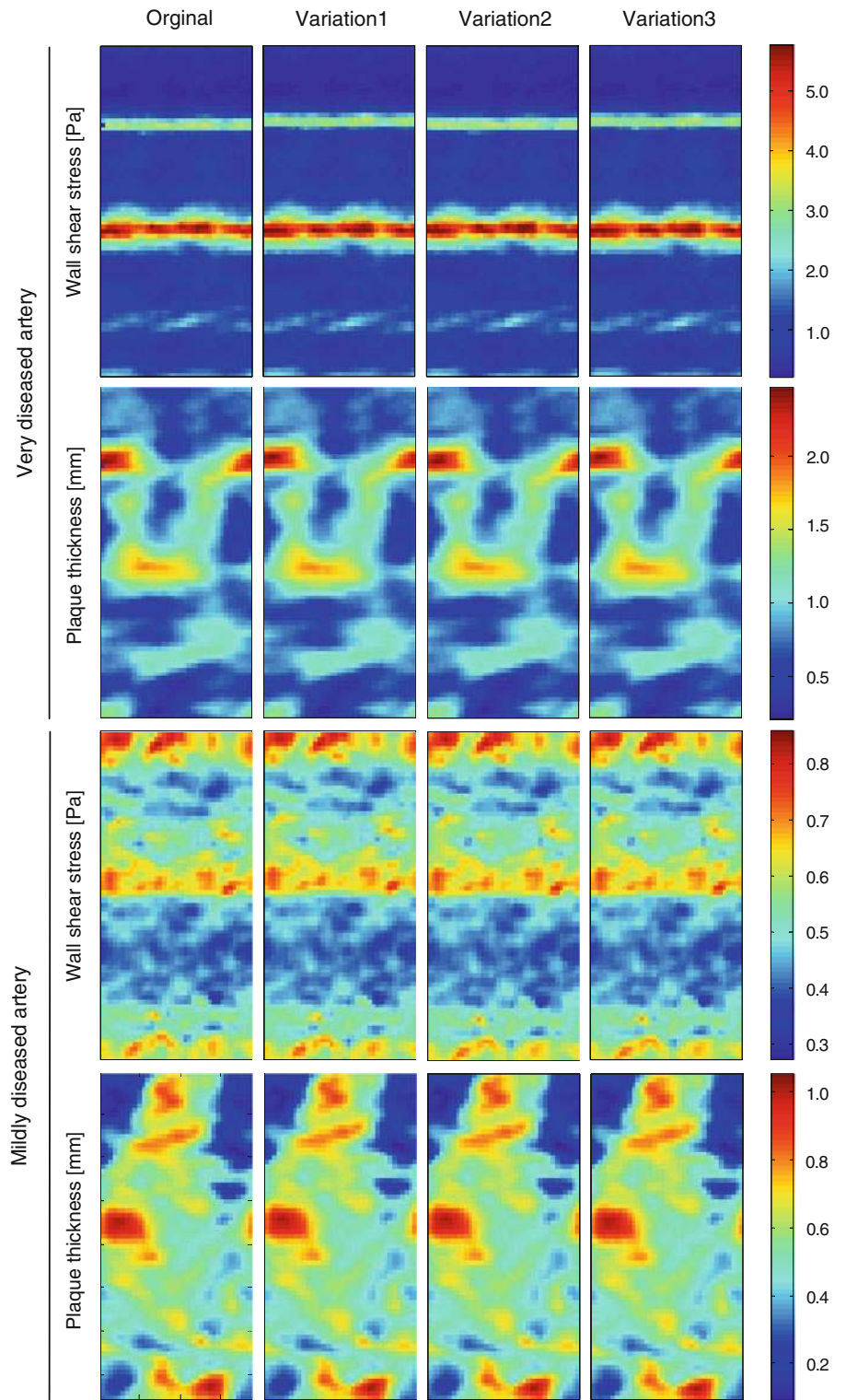
artery along its length. To obtain the WSS-PT relation, both are averaged over the length of the artery. These longitudinally averaged values are plotted and by regression analysis the relationship between WSS and PT can be determined, **a** indicates the slope and **b** the off-set

is suitable to study the relationship between WSS and atherosclerosis in clinical studies.

We evaluated the fusion approach by comparing an independent measure: the length of the two matched data sets. The results of this study show an excellent correlation between the two. Furthermore, variation in the selection of landmarks did not influence the patterns or spatially averaged values of WSS and plaque thickness. The method is more sensitive for landmark selection if we compare the results on a pixel-to-pixel basis, especially in severely stenosed arterial segments.

In many clinical studies, the influence of WSS on atherosclerosis was evaluated after applying spatially averaging of the parameters. In these studies, the relationship between WSS and plaque localization [6], plaque progression [24, 25], in stent restenosis [25–27] and plaque composition [28] was established. The results of this paper show that fusion of CT and IVUS is a suitable imaging alternative for these kind of studies. Absolute WSS values should, however, be regarded with caution since some assumptions such as discarding the side-branches and estimation of the inlet flow could influence these values.

Fig. 7 Absolute wall shear stress (WSS) and plaque thickness (PT) values. From left to right the original reconstruction and different variations are depicted. The two top panels give WSS and PT for the very diseased artery and the bottom two panels the WSS and PT for the mildly diseased artery



The influence of WSS on the vulnerable plaque is less well established, although several reviews were published in which possible mechanisms are presented [3–5, 24]. These mechanisms often involve local phenomena, and application of the current method kind of studies might occasionally lead to inaccuracies in WSS determination.

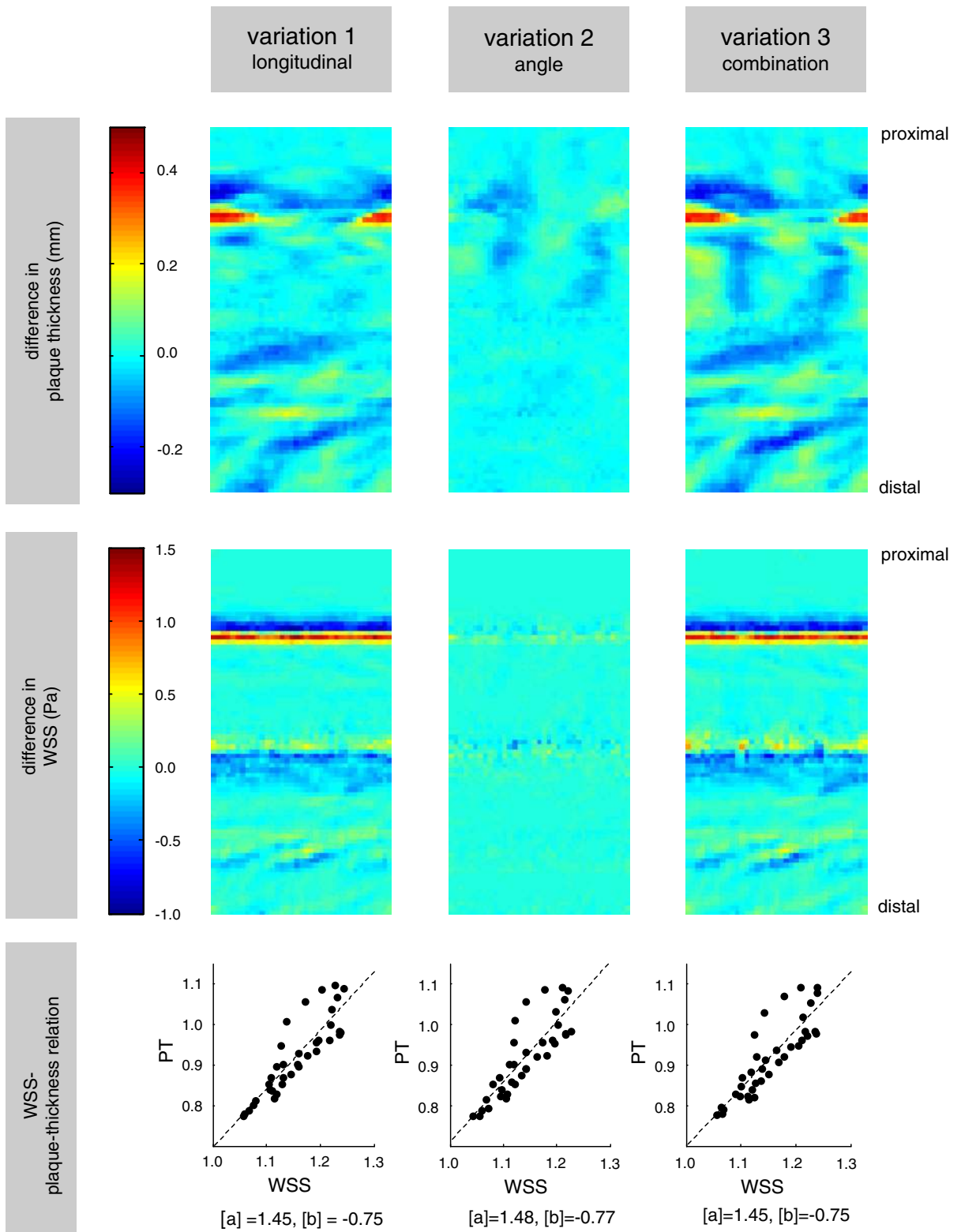
The other imaging procedure to generate a reliable 3D lumen and vessel wall reconstruction relies on the combination of biplane angiography and IVUS. This imaging technique, dubbed ANGUS [6, 26], was validated and used in many clinical investigations relating WSS to plaque thickness. Although the accuracy of the two methods are comparable (centerline reconstruction error in ANGUS $\sim 4\%$, in the current method 5%), there are also some differences. The main advantage of the ANGUS procedure is that the centerline and IVUS imaging are virtually simultaneous, and that the procedure does not rely on the selection and matching of anatomical landmarks. Furthermore, ANGUS does not require an additional (MSCT) imaging procedure. The main disadvantage of the ANGUS is that it required biplane angiography, which is not readily available, thus limiting the number of patients that can be investigated. Furthermore, it requires a sheath-based IVUS catheter which is not a necessity for the new procedure discussed in this paper. Finally, the current fusion method can be combined with lumen segmentation in the MSCT images, which opens up the possibility to include side branches—and thus coronary bifurcations—in future studies. Since atherosclerosis is often located near the bifurcations [2], accurate WSS values at these locations may provide valuable information.

Apart from application of WSS analyses, the current framework opens avenues for many other applications. Since the 3D position and orientation of the IVUS images are known, CT cross-sectional images can be generated at the same location. This allows slice-by-slice comparison of the IVUS and CT-cross-sectional images in which plaque characteristics can be compared. It is also possible to position the IVUS contours into the CT dataset (Fig. 4) and by this comparison we might be able to establish guidelines for quantifying lumen and plaque in CT. Once CT derived contours are available, either manually or automatically, the fusion also allows detailed comparison to the IVUS lumen and wall contours.

Fig. 8 Effect of variation on WSS analysis for the very diseased artery. For the diseased artery the absolute difference for the three variations are depicted for the plaque thickness and WSS. Despite some high local differences, the WSS-plaque-thickness-relation is not changed as result of the variations in fusion

The current framework could benefit from automation of the several observer dependent steps. At this moment the centerline is manually drawn, but it has been shown that automated centerline extraction is a reliable alternative [29, 30]. The selection of the landmarks is done on cross-sectional views and this will be hard to automate. A different approach to match the landmarks for the fusion is proposed by Marquering et al. [31]. Instead of matching in a cross-sectional view, they used maximum intensity plots in the longitudinal direction for both IVUS and MSCT and assessed the landmarks in these longitudinal views. Which approach results in the most accurate fusion, is most easy to apply and most easy to automate, needs to be investigated. Since the semi-automatic segmentation of the lumen and EEM is the most time consuming part of this technique, it would benefit from validated segmentation algorithms, which are to our knowledge not available yet. Automation of various steps in the procedure have the additional benefit that processing time will reduce considerably.

A second improvement concerns the length of the fused segments. The fused segments are relatively short, on average 36 mm. An IVUS pullback is for safety reasons also limited to a relative small part of the coronary tree. Since small side-branches are often not visible on CT, we rely on the large side-branches but at least two landmarks are necessary for the fusion procedure. Short IVUS segments therefore hinder the fusion over long parts. A third improvement concerns the extraction of the IVUS images from the complete pull-back. Ideally the images would be extracted in the same time-frame of the heart beat as the reconstruction of the CT images. In our method the IVUS images are extracted at end-diastole, while the CT is reconstructed during mid-diastole. However, the influence on the reconstruction is expected to be small, since the movement of the arteries during this cardiac phase are small. The short fused segments, in combination with the invasive nature of IVUS and the accompanying high costs, limit the wide assessment of the WSS influence on



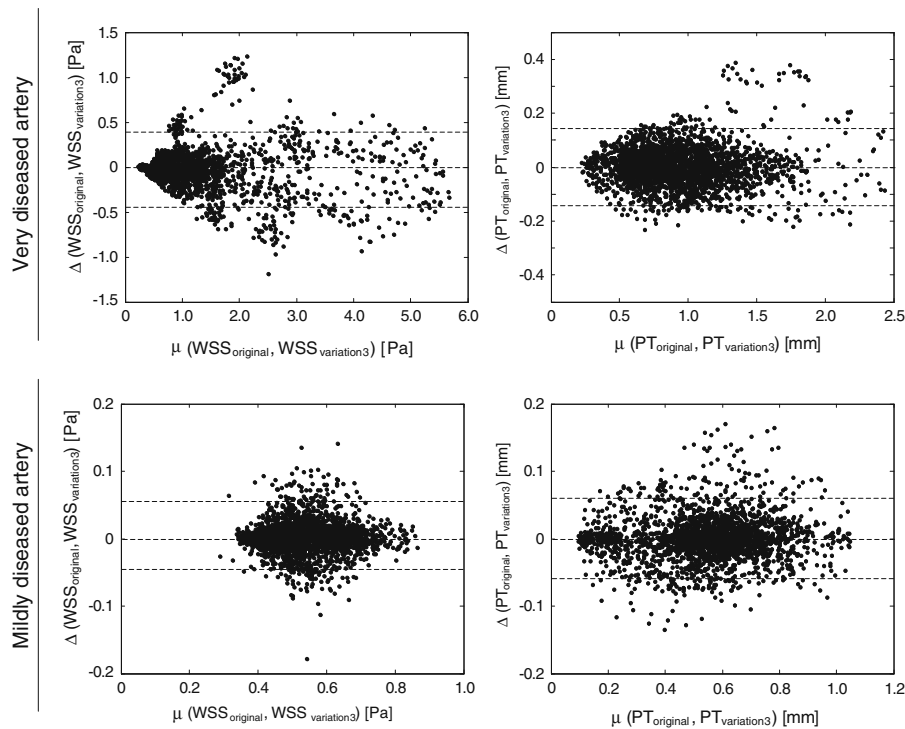


Fig. 9 Bland–Altman analysis of the wall shear stress (WSS) (left column) and plaque thickness (PT) (right column) for the comparison of the combined variation 3 and the original fusion.

At the top row the plots are depicted for the very diseased artery, at the bottom row for the mildly diseased artery

Table 1 Effect of the variations on plaque thickness location and the local wall shear stress

	Maximum PT (mm)	Location of maximum PT		WSS at maximum PT (Pa)
		mm	Angle	
Diseased				
Original	2.5	9.0	15	2.2
Variation 1	2.5	8.5	20	1.9
Variation 2	2.5	9.0	20	2.3
Variation 3	2.5	8.5	30	1.8
Mildly diseased				
Original	1.1	36.0	265	0.7
Variation 1	1.1	36.0	255	0.7
Variation 2	1.1	36.0	265	0.7
Variation 3	1.1	36.5	255	0.7

the atherosclerosis. Overall, it would be a step forward if CT could be used stand-alone to obtain lumen and wall information for WSS analysis. Since the resolution of CT is still improving and automated segmentation algorithms are under development and

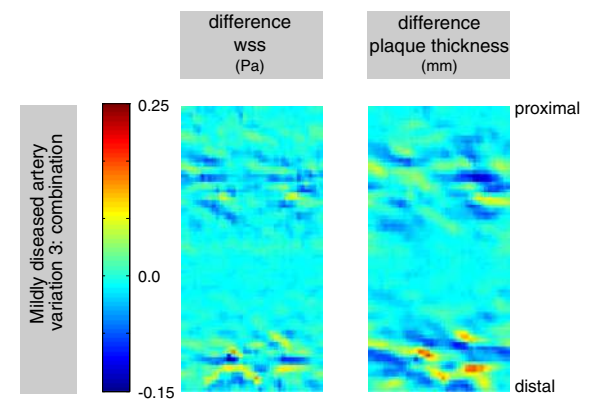


Fig. 10 Effect of variation on wall shear stress (WSS) analysis for the mildly diseased artery. For the healthy artery the absolute difference of the combined longitudinal and angular variation is shown for the wall shear stress and the plaque thickness. The graph shows the WSS-plaque-thickness-relation. The color bar is for both the WSS and the plaque thickness

under validation, WSS analysis in relation to risk prediction might be possible by using solely CT as imaging modality.

Table 2 Comparison between original fusion and fusion with variations

	Variation 1		Variation 2		Variation 3	
	R^2	95% CI	R^2	95% CI	R^2	95% CI
Diseased						
Plaque thickness (mm)	0.97	−0.13 to 0.12 −13.2 to 12.7%	0.99	−0.05 to 0.06 −5.8 to 6.0%	0.95	−0.14 to 0.14 −15.6 to 15.5%
WSS (Pa)	0.96	−0.45 to 0.40 −28.0 to 25.0%	1	−0.12 to 0.10 −6.9 to 5.9%	0.96	−0.45 to 0.40 −29.0 to 26.0%
Mildly diseased						
Plaque thickness (mm)	0.97	−0.06 to 0.06 −16.3 to 15.5%	0.99	−0.03 to 0.04 −6.1 to 3.6%	0.97	−0.06 to 0.06 −14.7 to 14.3%
WSS (Pa)	0.94	−0.05 to 0.05 −8.6 to 9.4%	0.98	−0.02 to 0.03 −4.4 to 4.7%	0.95	−0.04 to 0.05 −8.0 to 8.8%

In conclusion, the presented framework in which human coronary IVUS and CT are fused, can be used to derive 3D lumen and wall geometries in which the relationship between WSS and atherosclerosis can be investigated. Moreover, the framework opens avenues for validation of coronary segmentation algorithms from CT.

References

- Malek AM, Izumo S (1995) Control of endothelial cell gene expression by flow. *J Biomech* 28(12):1515–1528
- VanderLaan PA, Reardon CA, Getz GS (2004) Site specificity of atherosclerosis, site-selective responses to atherosclerotic modulators. *Arterioscler Thromb Vasc Biol* 24:1–11
- Slager CJ et al (2005) The role of shear stress in the generation of rupture-prone vulnerable plaques. *Nat Clin Pract Cardiovasc Med* 2(8):401–407
- Chatzizisis YS et al (2008) Prediction of the localization of high-risk coronary atherosclerotic plaques on the basis of low endothelial shear stress: an intravascular ultrasound and histopathology natural history study. *Circulation* 117(8):993–1002
- Slager CJ et al (2005) The role of shear stress in the destabilization of vulnerable plaques and related therapeutic implications. *Nat Clin Pract Cardiovasc Med* 2(9):456–464
- Krams R et al (1997) Evaluation of endothelial shear stress and 3D geometry as factors determining the development of atherosclerosis and remodeling in human coronary arteries in vivo. Combining 3D reconstruction from angiography and IVUS (ANGUS) with computational fluid dynamics. *Arterioscler Thromb Vasc Biol* 17(10):2061–2065
- Mowatt G et al (2008) 64-Slice computed tomography angiography in the diagnosis and assessment of coronary artery disease: systematic review and meta-analysis. *Heart* 94(11):1386–1393
- Mollet NR et al (2005) High-resolution spiral computed tomography coronary angiography in patients referred for diagnostic conventional coronary angiography. *Circulation* 112(15):2318–2323
- de Feyter PJ (2008) Multislice CT coronary angiography: a new gold-standard for the diagnosis of coronary artery disease? *Nat Clin Pract Cardiovasc Med* 5(3):132–133
- Frauenfelder T et al (2007) In-vivo flow simulation in coronary arteries based on computed tomography datasets: feasibility and initial results. *Eur Radiol* 17(5):1291–1300
- Suo J, Oshinski JN, Giddens DP (2008) Blood flow patterns in the proximal human coronary arteries: relationship to atherosclerotic plaque occurrence. *Mol Cell Biomech* 5(1):9–18
- Rybicki FJ et al (2009) Prediction of coronary artery plaque progression and potential rupture from 320-detector row prospectively ECG-gated single heart beat CT angiography: Lattice Boltzmann evaluation of endothelial shear stress. *Int J Cardiovasc Imaging* 25:289–299
- Leber AW et al (2005) Visualising noncalcified coronary plaques by CT. *Int J Cardiovasc Imaging (Formerly Cardiac Imaging)* 21:55–61
- Pohle K et al (2007) Characterization of non-calcified coronary atherosclerotic plaque by multi-detector row CT: comparison to IVUS. *Atherosclerosis* 190(1):174–180
- Achenbach S et al (2004) Assessment of coronary remodeling in stenotic and nonstenotic coronary atherosclerotic lesions by multidetector spiral computed tomography. *J Am Coll Cardiol* 43(5):842–847
- Leber AW et al (2005) Quantification of obstructive and nonobstructive coronary lesions by 64-slice computed tomography—a comparative study with quantification coronary angiography and intravascular ultrasound. *J Am Coll Cardiol* 26(1):147–154
- Mintz GS et al (2001) American College of Cardiology clinical expert consensus document on standards for acquisition, measurement and reporting of intravascular ultrasound studies (IVUS). A report of the American

- College of Cardiology task force on clinical expert consensus documents. *J Am Coll Cardiol* 37(5):1478–1492
18. Ropers U et al (2007) Influence of heart rate on the diagnostic accuracy of dual-source computed tomography coronary angiography. *J Am Coll Cardiol* 50(25):2393–2398
 19. Dewey M et al (2007) Influence of heart rate on diagnostic accuracy and image quality of 16-slice CT coronary angiography: comparison of multisegment and halfscan reconstruction approaches. *Eur Radiol* 17(11):2829–2837
 20. De Winter SA et al (2004) Retrospective image-based gating of intracoronary ultrasound images for improved quantitative analysis: the intelligate method. *Catheter Cardiovasc Interv* 61(1):84–94
 21. Seo T, Schachter LG, Barakat AI (2005) Computational study of fluid mechanical disturbance induced by endovascular stents. *Ann Biomed Eng* 33(4):444–456
 22. Doriot PA et al (2000) In-vivo measurements of wall shear stress in human coronary arteries. *Coron Artery Dis* 11(6):495–502
 23. Wentzel JJ et al (2005) Geometry guided data averaging enables the interpretation of shear stress related plaque development in human coronary arteries. *J Biomech* 38(7):1551–1555
 24. Chatzizisis YS et al (2007) Role of endothelial shear stress in the natural history of coronary atherosclerosis and vascular remodeling: molecular, cellular, and vascular behavior. *J Am Coll Cardiol* 49(25):2379–2393
 25. Wentzel JJ et al (2003) Extension of increased atherosclerotic wall thickness into high shear stress regions is associated with loss of compensatory remodeling. *Circulation* 108(1):17–23
 26. Wentzel JJ et al (2001) Relationship between neointimal thickness and shear stress after Wallstent implantation in human coronary arteries. *Circulation* 103(13):1740–1745
 27. Stone PH et al (2003) Effect of endothelial shear stress on the progression of coronary artery disease, vascular remodeling, and in-stent restenosis in humans: in vivo 6-month follow-up study. *Circulation* 108(4):438–444
 28. Gijssen FJ et al (2008) Strain distribution over plaques in human coronary arteries relates to shear stress. *Am J Physiol Heart Circ Physiol* 295(4):H1608–H1614
 29. Metz CT et al (2007) Semi-automatic coronary artery centerline extraction in computed tomography angiography data. In: *IEEE international symposium on biomedical imaging: Macro to Nano*
 30. Schaap M et al (2009) Standardized evaluation methodology and reference database for evaluating coronary artery centerline extraction algorithms. *Med Image Anal* 13(5):701–714
 31. Marquering HA et al (2008) Coronary CT angiography: IVUS image fusion for quantitative plaque and stenosis analyses. In: *Medical imaging 2008: visualization, image-guided procedures, and modeling*. Proceedings of the SPIE